Movers and Shakers: Kinetic Energy Harvesting for the Internet of Things

Maria Gorlatova, John Sarik, Guy Grebla, Mina Cong, Ioannis Kymissis, *Senior Member, IEEE*, and
Gil Zussman, *Senior Member, IEEE*

Abstract—**Numerous energy harvesting wireless devices that will serve as building blocks for the Internet of Things (IoT) are currently under development. However, there is still only limited understanding of the properties of various energy sources and their impact on energy harvesting adaptive algorithms. Hence, we focus on characterizing the kinetic (motion) energy that can be harvested by a wireless node with an IoT form factor and on developing energy allocation algorithms for such nodes. In this paper, we describe methods for estimating harvested energy from acceleration traces. To characterize the energy availability associated with specific human activities (e.g., relaxing, walking, cycling), we analyze a motion dataset with over 40 participants. Based on acceleration measurements that we collected for over 200 hours, we study energy generation processes associated with day-long human routines. We also briefly summarize our experiments with moving objects. We develop energy allocation algorithms that take into account practical IoT node design considerations, and evaluate the algorithms using the collected measurements. Our observations provide insights into the design of motion energy harvesters, IoT nodes, and energy harvesting adaptive algorithms.**

Index Terms—**Energy harvesting, motion energy, measurements, low-power networking, algorithms, Internet of Things.**

I. Introduction

ADVANCES in the areas of solar, kinetic, and thermal energy harvesting as well as in low-power wireless communications will soon enable the realization of *self-sustainable wireless devices* [2]–[5]. These devices can compose networks of rechargeable sensors [4], [5], active tags [3], or computational RFIDs [6]. Such networks will serve as building blocks for emerging Internet-of-Things (IoT) applications, including supply chain management and wearable computing.

Two promising energy sources for IoT nodes are *light and motion*.[1] Accordingly, extensive effort has been dedicated to the design of solar cells and kinetic energy harvesters (e.g., [8]–[11]). Moreover, the design of energy harvesting-adaptive communication and networking algorithms recently gained extensive attention [4], [12]–[15]. To complement these efforts, [5], [13], [16] collected traces and studied the impact of the *energy source properties* on higher layer algorithms. However, there is still only limited understanding of motion energy availability and its impact on the design of both hardware (energy harvesters, energy storage components) and algorithms. Moreover, commercially available harvesters are still not designed for human motion. Hence, we focus on *characterizing the kinetic (motion) energy that can be harvested by an IoT node and on the impact of the energy characteristics on harvesting adaptive algorithms*. Self-sustainable IoT nodes powered by motion will be implemented in ultra-low-power architectures. Thus, we additionally focus on *developing algorithms that take practical IoT node design considerations into account*.

Everyday activities such as walking can generate substantial power [17]. Therefore, many harvesters are under development, including shoe inserts that harvest energy from footfalls [8] and mobile phone chargers integrated in backpacks [10] or phones [9]. While there are several ways of harvesting motion energy, we focus on *inertial energy harvesters*, since their form factor fits IoT applications. An inertial harvester suitable for a small wireless device (e.g., under 5 cm × 5 cm, and weighing less than 2 grams) can generate 100–200 μW from walking [18], [19], which is sufficient for many applications.[2] However, the harvesting level changes dynamically as illustrated in Fig. 3 that shows the power harvesting level corresponding to a device carried by a walking person.

In inertial harvesters, the output power is maximized when the harvester resonant frequency is "matched" to the motion frequency [11] (see Section IV for details). Human motion is a combination of low frequency vibrations (< 10 Hz) that vary from activity to activity and from person to person. Therefore, characterizing the properties of the harvested power requires an in-depth study of human motion (e.g., the frequencies associated with different motions) and human mobility patterns. Namely, characterizing kinetic energy harvesting is

---

[1]The power available from *RF harvesting* is *100 times less than the power available from indoor light* [7]. *Thermal gradients* can provide substantial power in industrial applications, but are currently impractical for non-industrial IoT applications.

[2]This is comparable to the power a solar cell of similar size can harvest from indoor light [5], [13].

substantially more complex than characterizing light energy harvesting (e.g., [13]).

We first describe methods for collecting *motion acceleration traces* and the methods of [11], [16], [19] for estimating harvested power from the traces. Our study is based on traces that we collected using SparkFun ADXL345 boards[3] and traces collected in [20] using similar devices. While the traces in [20] were collected to examine activity recognition, we use them to estimate the amount of energy that could be harvested. Moreover, while we focus on inertial harvesters, the traces that we collected (and that are shared via CRAWDAD [21]) *can be used with other harvester models*.

We examine the energy availability associated with *specific human motions*, such as walking, running, and cycling. Unlike previous studies that obtained estimates based on small numbers of participants [18], [19], [22], we use a motion dataset *with over 40 participants* [20], obtaining extensive and general kinetic energy characterization for common human motions. The study demonstrates the range of motion frequencies and harvested powers for different participants and activities, and *uniquely demonstrates the importance of human physical parameters for energy harvesting*. For example, the taller half of the participants can harvest on average 20% more power than the shorter half.

The *short duration* traces in [20] are for *specific motions*. To study the energy generation processes associated with *day-scale human routines* (as opposed to specific motions), we conducted a measurement campaign with 5 participants over a total of 25 days. We collected traces with over 200 hours of acceleration information for normal human routines. The traces provide important input for IoT node design (e.g., for determining the battery capacity and harvester size necessary for self-sustainable operation) and for algorithm design (as will be discussed below). Hence, *we share the collected dataset in* [23] and *via CRAWDAD* [21].[4] We analyze the traces and show that the power availability from normal routines and from indoor lights are comparable. We also demonstrate that the power generation process associated with human motion is highly variable. We compare this process with i.i.d. and Markov processes, demonstrating the importance of evaluating algorithms with real world traces and of developing algorithms that do not build on the adsumption that energy generation is Markovian or i.i.d.

We note that the primary goal of collecting and analyzing traces is to set a reasonable upper bound on the available energy and to study the energy availability dynamics. Commercially available kinetic energy harvesters [24]–[26] are optimized for harvesting energy from machine vibrations above 40 Hz. Therefore, these harvesters would generate essentially no energy when subjected to human motion. In general, measuring acceleration is preferable to measuring the energy harvested by a particular harvester, since the traces can be used to calculate how much energy any past, present, or future harvester would generate.

As the IoT will incorporate many objects, we additionally briefly present results regarding measurements with a variety of *moving objects*. For example, we measured the power that can be harvested from everyday activities such as writing with a pencil and opening a door. We also collected measurements for objects in transit. We shipped a FedEx box with a measurement unit across the U.S., placed a unit in a checked-in luggage during a 3 hour flight, and carried units on cars and trains. We confirm that, as expected based on inertial harvesters' *filter properties* (see Section III-A), the energy availability is low for many common non-periodic motions. We additionally demonstrate that the energy availability is low for many *high-amplitude periodic object motions*. For example, we show that inertial harvesters can harvest little energy from opening and closing a door, opening cabinet drawers, and spinning a swivel chair.

Next, we develop *energy allocation algorithms* for wireless IoT nodes. Due to the high variability of energy obtained from motion, IoT nodes that harvest this energy will implement algorithms that control the node's *energy spending rates* [4], [12]–[14], [27], [28]. The spending rates will provide inputs for determining node transmission power, duty cycle, sensing rate, or communication rate. We formulate an optimization problem of a node whose objective is to *maximize the utility of its energy allocations*, and develop algorithms for solving it. The problem formulation and the algorithms take into account *realistic properties of an ultra-low-power IoT node* and based on our measurement observations do not make assumptions regarding the harvesting process.

In particular, IoT nodes that are powered by the motion energy will likely to be implemented in *ultra-low-power architectures*. As such, they will support only a limited number of possible energy spending rates, and their energy use patterns may call for considering various possible utility functions. Moreover, these nodes will likely to use *capacitors* [6], [13], [29], rather than *batteries*, as their energy storage components. This is due to the fact that capacitors can be charged and discharged many more times than batteries, which is an important feature for nodes powered by the widely varying motion energy. Additionally, capacitors are more environmentally friendly than batteries [6], and are therefore more suitable for human-facing IoT applications such as wearable computing. To the best of our knowledge, these aspects of IoT node modeling have not been jointly considered before.

For solving the energy allocation problem, we develop an optimal offline algorithm, an efficient approximation scheme, and an online algorithm which is optimal in certain cases. We evaluate the algorithms using the collected measurement traces. The evaluation results demonstrate that the approximation and online algorithms perform well and highlight the importance of designing algorithms that take into account the energy storage properties of the IoT nodes.

To summarize, the main contributions of this paper are: (i) insights into energy availability from human motion, based on a dataset with a large number of participants, (ii) collection of a dataset of long-term human motion and a study of the corresponding energy generation processes, and (iii) energy allocation algorithms that take practical IoT node design considerations into account. The collected motion traces are already

---

[3]Although smartphones include accelerometers, we use dedicated sensing units, since the phones' accelerometers have a limited range, restricted sampling rate control, and high energy consumption (that hinders day-scale trace collection).

[4]To the best of our knowledge, this is the first publicly available long-term human motion acceleration dataset.

available online [23]. The paper contributes to the understanding of motion energy harvesting availability and properties, and provides insights that are important for the design of motion energy harvesters, IoT nodes, and energy harvesting adaptive algorithms.

The paper is organized as follows. Section II summarizes the related work and Section III describes the harvester model, the measurements, the procedures for determining the harvester parameters, and the wireless node model. Section IV focuses on common human motions and Section V focuses on our measurement campaign and day-scale human motion measurements. Additionlly, Section V provides brief comments regarding motion of objects. Section VI describes our algorithms and provides the results of algorithm evaluations with the collected measurements. Section VII concludes the paper.

II. RELATED WORK

To the best of our knowledge, our experiments with long-term activities (Section V-A) and with object motion (Section V-C) are unique. Below we briefly summarize the related work for our other contributions.

Previous studies that examined energy of *particular human motions* had a small number of participants (10 in [18] and 8 in [16], [19]). Additionally, with the exception of [16], they examined short intervals of walking and running on a treadmill at a constant pace. We examine a dataset [20] with over 40 participants performing a set of several unrestricted motions[5] and *labeled with human physical parameters*. To the best of our knowledge, this is the first publicly available acceleration dataset collected for a large number of participants. It *was not previously used for an energy study*.

Day-scale human motion acceleration traces were previously collected for 8 participants over 3 days and examined in [16], which established energy budgets for wearable nodes using assumptions suitable for larger electronic devices. The data collected in [16] is not publicly available. We collect day-scale data that in some cases has more information per participant, examine the traces under assumptions suitable for small IoT nodes, and characterize energy harvesting process variability and properties that *have not been considered before*.

Many energy harvesting adaptive communication and networking algorithms have been recently developed (e.g., [4], [12], [14], [15], [27], [28], [31]–[34]). We consider a wireless node model and develop algorithms that capture several practical IoT node design aspects: (i) *discrete*, rather than continuous [12]–[15], [27], energy spending rates; (ii) *general*, rather than concave [12]–[15], [27] or linear [4], utility functions; and (iii) use of a *capacitor* [13], [29], rather than a battery [12], [14], [15], [27], as an energy storage component. These aspects have not been jointly considered before. Existing algorithms are typically evaluated with light [4], [12], [29] or wind [12] energy traces. We evaluate the algorithms with the collected day-scale human motion energy measurements.

TABLE I
NOMENCLATURE

|	
m	Harvester proof mass [kg]
Z_L	Harvester proof mass displacement limit [m]
k	Harvester spring constant [kg·s^2]
b	Harvester damping factor [kg/s]
f_r	Harvester resonant frequency [Hz]
f_m	Dominant motion frequency [Hz]
$a(t)$	Acceleration [m/s^2]
D	Absolute deviation of acceleration [m/s^2]
$P(t)$	Power [W]
$z(t)$	Proof mass displacement [m]
i, K	Time slot index and a number of time slots
$s(i)$	Energy spending rate [J/slot]
$\mathcal{S}$	Set of feasible $s(i)$ values
$r(i)$	Data rate [Kb/s]
$U(s(i))$	Utility function
$B(i)$	Energy storage level [J]
$e(i)$	Environmental energy level [J]
$Q(e(i), B(i))$	Energy harvesting rate [J/slot]
$L(i, B(i))$	Energy loss (leakage) rate [J/slot]
$\eta(i, B(i))$	Energy conversion efficiency [dimensionless]
C	Energy storage capacity [J]
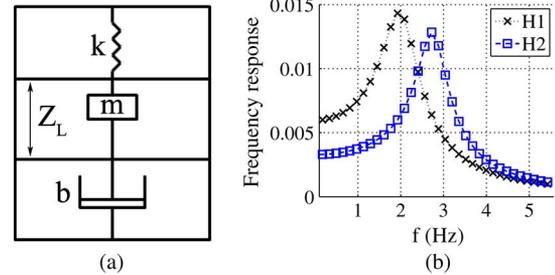
Fig. 1. (a) A *second-order mass-spring system model* of a harvester with proof mass m, proof mass displacement limit Z_L, spring constant k, and damping factor b, and (b) the frequency response magnitude for harvesters $H1$ and $H2$.

III. MODELS AND MEASUREMENT SETUP

Our motion energy study is based on recorded *acceleration* traces which are processed, following the methods developed in [11], [16], [19], to determine the energy generated by an inertial harvester. Our algorithms are developed based on a model that extends existing models [4], [12]–[14], [27] to capture important IoT node design considerations. In this section, we describe the kinetic energy harvester model, the collection of acceleration measurements, the procedures for determining the harvester parameters, and the wireless node model. The notation is summarized in Table I.

A. Inertial Harvester Model

An inertial harvester can be modeled as a second-order mass-spring system with a harvester proof mass m, proof mass displacement limit Z_L, spring constant k, and spring damping factor b [11], [19]. Fig. 1(a) demonstrates such a harvester model.

Two important *harvester design parameters* are m and Z_L. The harvester output power, P, increases linearly with m [35], and is non-decreasing (but generally non-linear) in Z_L. Yet, m and Z_L are limited by the harvester weight and size considerations, which ultimately depend on the application. We use the following values that are consistent with the IoT restrictions on the size and weight of a node, and correspond to one of

---

[5]The properties of restricted and unrestricted human motions are known to differ [30].
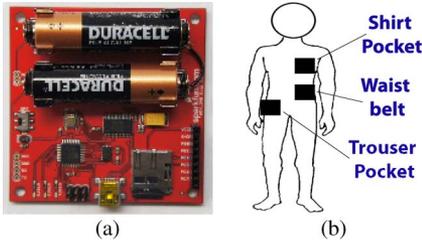
Fig. 2. Acceleration measurement unit and placements: (a) our sensing unit based on a SparkFun ADXL345 board, and (b) the sensing unit placements in a multi-participant human motion characterization study [20].

the configurations examined in [19]: (i) $m = 1 \cdot 10^{-3}$ kg and (ii) $Z_L = 10$ mm.

The other two model parameters, k and b, are tuned to optimize the energy harvested for given motion properties. The parameter k determines the *harvester resonant frequency*, $f_r = 2\pi\sqrt{k/m}$. To maximize power output, *the resonant frequency, f_r, should match, reasonably closely, the dominant frequency of motion, f_m*.

Jointly, k and b determine the *harvester quality factor*, $Q = \sqrt{km}/b$, which determines the spectral width of the harvester. A harvester with a small Q harvests a wide range of frequencies with a low peak value, while a harvester with a large Q is finely tuned to its resonant frequency f_r. The role of f_r and Q can be observed in Fig. 1(b), which shows the magnitude of the frequency response of two different harvesters, denoted by $H1$ and $H2$. For $H1$, $f_r = 2.06$ Hz (which corresponds to a typical frequency of human walking) and $Q = 2.35$ ($k = 0.17$, $b = 0.0055$). For $H2$, $f_r = 2.77$ Hz (which corresponds to a typical frequency of human running) and $Q = 3.87$ ($k = 0.30$, $b = 0.0045$).

B. Collecting Motion Information

In Sections IV–VI, we examine measurements that we collected and measurements provided in a triaxial acceleration dataset of common human motions [20]. Our measurements were obtained with sensing units based on SparkFun ADXL345 evaluation boards (see Fig. 2(a)). Each unit includes an ADXL345 tri-axis accelerometer, an Atmega328P microcontroller, and a microSD card for data logging. The sensing units record acceleration along the x, y, and z axes, $a_x(t)$, $a_y(t)$, $a_z(t)$, with a $+/-16g$ range and a 100 Hz sampling frequency. We conducted multiple experiments with multiple sensing unit placements, as described in Section V.

The dataset of [20] was obtained using an ADXL330 tri-axis accelerometers with a 100 Hz sampling frequency. The measurements of [20] were conducted with sensing unit placements corresponding to a shirt pocket, waist belt, and trouser pocket, as shown in Fig. 2(b). These placements on the human torso are used by people carrying different objects (e.g., keys, sunglasses, wallet). In all the measurements, the orientation of the sensing unit is not controlled. We examine $a(t) = \sqrt{a_x(t)^2 + a_y(t)^2 + a_z(t)^2}$, the overall magnitude of the acceleration. Due to the earth gravity of 9.8 m/s² ("1g"), the measured acceleration includes a constant component that we filter out (similarly to [16], [19], we use a 3rd order Butterworth high-pass filter with a 0.1 Hz cutoff frequency).
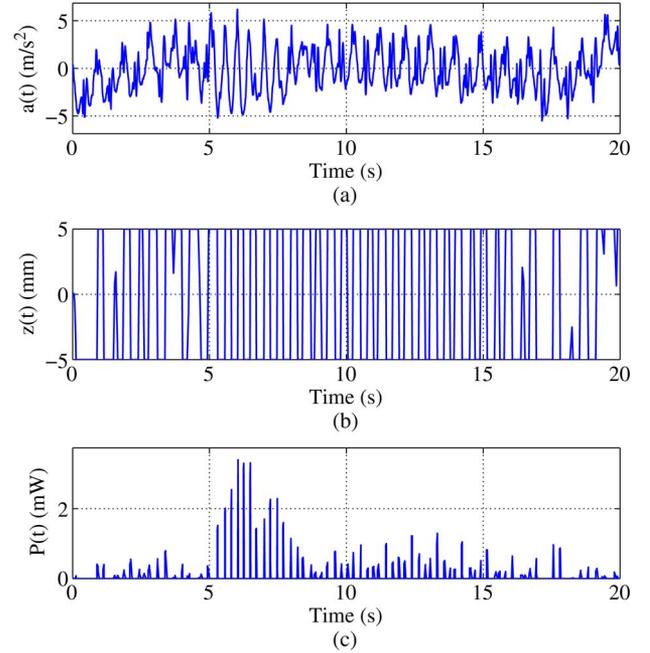

Fig. 3. Demonstration of obtaining the power generated by a harvester, $P(t)$, from the recorded acceleration, $a(t)$: (a) $a(t)$ recorded by aperson walking, (b) the corresponding harvester proof mass displacement, $z(t)$, and (c) the resulting $P(t)$ for harvester $H1$ ($k = 0.17$, $b = 0.0055$).

We examine two motion properties of the measurements: the *average absolute deviation of the acceleration*, D, and the dominant frequency of motion, f_m. D quantifies the variability in the $a(t)$ value and is a measure of the "amount of motion." It is calculated as $D = \frac{1}{T}\sum_T (a(t) - \bar{a}(t))$, where $\bar{a}(t)$ denotes the average of $a(t)$ over time interval T. We obtain f_m by determining the maximum spectral component of the Fourier Transform of $a(t)$.

C. Harvesting Rates and Data Rates

We calculate the power generated by a harvester, $P(t)$, subjected to acceleration $a(t)$, using the following procedure based on the methods developed in [16]. We first convert $a(t)$ to proof mass displacement, $z(t)$, using the Laplace-domain transfer function

$$z(t) = \mathcal{L}^{-1}\{z(s)\} = \frac{a(s)}{s^2 + (2\pi f_r/Q)s + (2\pi f_r)^2}.$$

Next, to account for Z_L, we limit $z(t)$ using a Simulink limiter block. The power $P(t)$ generated by the harvester is then determined as $P(t) = b(dz(t)/dt)^2$. The average of $P(t)$ is denoted by $\bar{P}$.

We implemented this procedure in MATLAB and Simulink. Fig. 3 shows an example of obtaining $P(t)$ for a particular $a(t)$. The $a(t)$ values were recorded by a sensing unit carried by a walking person (Fig. 3(a)), and the $z(t)$ and $P(t)$ values were obtained using the procedure described above for the harvester $H1$.

To characterize the performance of wireless IoT nodes, we calculate the data rates, $\bar{r}$, that a node would be able to maintain when harvesting the generated $\bar{P}$. The harvester energy conversion efficiency, η_h, depends on various factors [24] (e.g.,
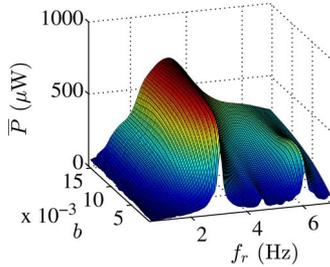
Fig. 4.   The average power generated by a harvester, $\overline{P}$, from the same motion (human running) for different combinations of harvester resonant frequencies, f_r, and damping factors, b.

selected regulated output and temperature). While perfectly optimized energy harvesting systems obtain energy conversion efficiency values between 30% and 90% [36], we use $\eta_h = 20\%$ which is more realistic for practical systems where the harvester cannot be continuously aligned with the axis that generates the maximum output throughout the day. Similar to [13], we assume that the communication cost is $c_{tx} = 1$ nJ/bit for ultra-low-power transceivers appropriate for IoT nodes. Hence, $\overline{r} = \eta_h \overline{P}/c_{tx} = 2 \cdot 10^5 \overline{P}$ (Kb/s).

D. Optimizing the Harvester Parameters

Finding the optimal harvester parameters k and b is difficult because it requires optimizing over a multi-dimensional surface of unknown geometry [19]. For example, Fig. 4 shows the average power ($\overline{P}$) values calculated from a set of $a(t)$ measurements (corresponding to a person running) for different f_r and b combinations. To determine the optimal harvester parameters for short $a(t)$ samples, we implemented an *exhaustive search* algorithm. The algorithm considers a large number of k and b combinations, obtains the corresponding $\overline{P}$ (using the procedure described in Section III-C), and chooses the k and b combination that maximizes $\overline{P}$.

The exhaustive search algorithm is time-consuming even for relatively short $a(t)$ samples. For longer $a(t)$ samples, we implemented a simplified procedure developed in [16]. The procedure first determines the k value that matches the harvester's f_r to the dominant frequency in the $a(t)$ sample, f_m. Specifically, the procedure selects k such that $k = m f_r^2/(2\pi)^2 = (m f_m^2)/(2\pi)^2$. It then considers a relatively large number of b values and selects the b that maximizes $\overline{P}$.

E. Wireless Node Model

We model an ultra-low-power IoT node that harvests energy, stores it in an energy storage device, and uses it to communicate wirelessly (e.g., a wearable node may be communicating with a human-carried mobile phone). We assume that the time is slotted and denote the slot index by i and the number of slots by K. We will develop algorithms that control the node energy spending rates, $s(i)$, which can provide inputs for determining node transmission power, duty cycle, sensing rate, or communication rate. An IoT node is likely to support only a restricted number of modes of operation (i.e., sleep, idle), transmission power

levels,[6] and transmission rates, thereby supporting only a finite set $\mathcal{S}$ of $s(i)$ values. We thus *restrict* $s(i)$ as $s(i) \in \mathcal{S} \cup \{0\}$ (note that $s(i)$ is typically modeled as a continuous variable [13], [27], [37]). This complicates the energy allocation problems, as we will demonstrate in Section VI-A.

We formulate an optimization problem for a single node which maximizes *the sum of the utilities of its per-time-slot energy allocations*. This problem is important, for example, in networks where nodes transmit mostly ID information [38] to a common gateway.[7] We consider a utility function $U(s(i))$ that corresponds to the *data rate $r(i)$ obtained when the energy spending rate is $s(i)$.*[8] The node may achieve different $r(i)$ in a slot i by transmitting different number of packets, changing the transmission power, or changing the packet size. Thus the utility function, U, may be *concave* (when the node changes its transmission power [15], [27], [37]), *linear* (when it transmits different number of packets), *convex* (when it changes the packet size under certain settings [39]), or *not concave and not convex* (when it changes a combination of the parameters). Correspondingly, *we place no restrictions on $U(s(i))$ except that it can be computed efficiently*.

An IoT node may use a *battery* or a *capacitor* as its energy storage device. For a slot i of duration T_{int}, $B(i)$ is the node energy storage level, $e(i) = \int_{t=iT_{int}}^{(i+1)T_{int}} P(t) dt$ is the environmental energy available to the node, and $L(i, B(i))$ is the energy loss (leakage) from the storage. $Q(e(i), B(i))$ is the energy harvested by the node; its dependency on $B(i)$ is characteristic of capacitor-based nodes [13], [40]. $\eta(i, B(i))$ is the *energy conversion efficiency* and C is the storage capacity. Between time slots, the energy storage evolves as

$$B(i) = \min\{B(i-1) + Q(e(i-1), B(i-1)) - L(i-1, \\ B(i-1)) - s(i-1)/\eta(i-1, B(i-1)), C\}.$$

$\eta(i, B(i))$ depends on the difference between the energy storage voltage, $V_{out}(i)$, and the node's operating voltage, V_{op}. Within a *battery*'s operating region, $V_{out}(i)$ is nearly constant. For a *capacitor*, $V_{out}(i)$ depends on $B(i)$ [13], [40]. We define two node models: for a *battery model*, $\eta(i, B(i)) = 1$, while for a *capacitor model*, $\eta(i, B(i))$ is a non-linear function. The $\eta(i, B(i))$ that we use in the performance evaluations is described in Section VI-C.

IV. HUMAN MOTION

We now examine a dataset with over 40 participants performing 7 common motions in unconstrained environments. We emphasize that this dataset, previously used to examine techniques for activity recognition [20], *has not been used for energy characterization*. We first introduce the study. Then, we characterize the energy availability for different motions, the

---

[6]For example, the ultra-low-power Chipcon CC1000, Chipcon CC2420, and Nordic NRF24L01 RF transceivers support, correspondingly, only 32, 8, and 4 transmission power levels.

[7]Single node energy allocation problems were studied in [13], [15], [27] under simpler models. In Section VI-A we show that even for a single node, the considered optimization problem is NP-hard. The extension to the case of multiple nodes is a subject for future research.

[8]The model allows $U(s(i))$ to account for other considerations as well (e.g., the number of activations of nodes' sensors when the energy spending rate is $s(i)$).
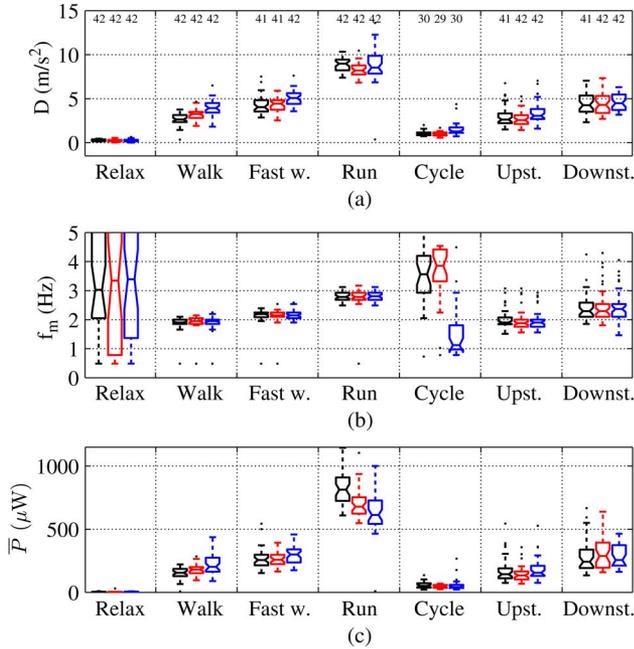
Fig. 5. Characterization of kinetic energy for common human activities, based on a 40-participant study: (a) average absolute deviation of acceleration, D, (b) dominant motion frequency, f_m, and (c) power harvested by an optimized inertial harvester, $\overline{P}$.

variability in motion properties among sensing unit placements and participants, and the dependence of energy availability on the participant's physical parameters.

A. Study Summary

The dataset we examine [20] contains motion samples for 7 common human activities—relaxing, walking, fast walking, running, cycling, going upstairs, and going downstairs—performed by *over 40 participants* and recorded from the 3 sensing unit placements, shown in Fig. 2(b). For each 20-second motion sample, we use the acceleration, $a(t)$, trace to calculate D, f_m, $\overline{P}$, and r. To obtain $\overline{P}$, we use the exhaustive search harvester optimization algorithm described in Section III-D. By determining the best harvester for each motion, we can offer important insights into the harvester design.

To validate the data from [20], we replicated the measurements using our sensing units. The results of our measurements were consistent with the provided data. We note that the f_m values calculated for the different motions in the dataset are consistent with the physiology of human motion. For example, the range of the calculated f_m values for running motion samples in the dataset corresponds to the typical foot strike cadence for running (180 foot strikes per minute, i.e., $f_m = 3$ Hz, is considered an optimal running cadence [41]).

The statistics of the calculated D, f_m, and $\overline{P}$ are summarized in the boxplots in Fig. 5. For each of the 7 motions the leftmost (black), middle (red), and rightmost (blue) boxes correspond to the *shirt pocket*, *waist belt*, and *trouser pocket* sensing unit placements, respectively. For each motion and sensing unit placement, the number of participants that had $a(t)$ samples appears on the top of Fig. 5(a). At each box, the central mark is the median, the edges are the 25th and 75th percentiles, the "whiskers" cover 2.7σ of the data, and the outliers are plotted

individually. In Table II we separately summarize the results for 4 important motions.

B. Energy for Different Activities

Relaxing: As expected, almost no energy can be harvested when a person is not moving ($\overline{P} < 5\ \mu$W).

Walking and Fast Walking: Walking is the predominant periodic motion in normal human lives and thus particularly important for motion energy harvesting. For walking, the median $\overline{P}$ is 155 μW for shirt pocket sensing unit placement, 180 μW for waist belt placement, and 202 μW for trouser pocket placement. These $\overline{P}$ values are in agreement with previous studies of energy harvesting for human walking [18], [19]. In comparison, *indoor light energy* availability is on the order of 50–100 μW/cm². Considering harvester energy conversion efficiency estimates [13], [16], *a similarly sized harvester would harvest more energy from walking than from indoor light*. Fast walking (identified as "fast" by the participants themselves) has higher D and f_m than walking at a normal pace (Fig. 5) and generates up to twice as much $\overline{P}$.

Running: Running, an intense repetitive activity, is associated with high D and f_m (Fig. 5(a) and (b)), and hence results in $612 \leq \overline{P} \leq 813\ \mu$W.

Cycling: For the examined unit placements, cycling generates relatively little energy—the median $\overline{P}$ values are 41–52 μW, 3.7–3.9 times less than the $\overline{P}$ for walking. While the high cadence of cycling motion results in relatively high f_m (Fig. 5(b)), a harvester not on the legs will be subject to only small displacements, resulting in small values of D (Fig. 5(a)) and $\overline{P}$ (Fig. 5(c)). For cycling-specific IoT applications, *harvester placements on the lower legs should be considered*.

Walking Upstairs and Downstairs: Comparing the $\overline{P}$ values for relaxing, walking, and running, one may conclude that higher exertion (perceived effort and energy expenditure) corresponds to higher energy harvesting rates. Our examination of walking upstairs and downstairs demonstrates that this is not the case. While people exert themselves more going upstairs, the $\overline{P}$ for going downstairs is *substantially higher than for going upstairs*, with the median $\overline{P}$ values differing by 1.65–2.1 times depending on the sensing unit placement. Although counterintuitive, going downstairs is associated with higher magnitudes of motion and higher motion frequencies (Fig. 5(a) and (b)), which leads to the higher $\overline{P}$. We observed the disconnect between perceived effort and energy harvesting rates in other measurements as well. For example, in our measurements highly strenuous push-ups and sit-ups resulted in lower $\overline{P}$ than non-strenuous walking at a normal pace.

C. Consistency of Dominant Motion Frequency

To maximize power output, the resonant frequency of a harvester, f_r, should "match" the dominant frequency of motion, f_m. In this section, we comment on the variability in f_m and provide important observations for harvester design. Due to space constraints, we leave the study of harvester sensitivity to different design parameters to future work.

Consistency Among Sensing Unit Placements: The same motion will result in a different f_m depending on the sensing

TABLE II
ENERGY BUDGETS AND DATA RATES BASED ON MEASUREMENTS OF COMMON HUMAN ACTIVITIES

Activity	Sensing unit placement	# subjects	Median f_m (Hz)	$\overline{P}$ (μW)			Median r (Kb/s)
				25th percentile	Median	75th percentile	
Relaxing	Trouser pocket	42	N/A	1.0	3.1	4.8	0.6
	Waist belt	42	N/A	0.3	2.4	4.8	0.5
	Trouser pocket	42	N/A	0.2	1.4	5.9	0.3
Walking	Shirt pocket	42	1.9	128.6	155.2	186.0	31.0
	Waist belt	42	2.0	151.8	180.3	200.3	36.0
	Trouser pocket	42	2.0	163.4	202.4	274.5	40.4
Running	Shirt pocket	42	2.8	724.2	813.3	910.0	162.6
	Waist belt	41	2.8	623.5	678.3	752.8	135.6
	Trouser pocket	42	2.8	542.3	612.7	727.4	122.5
Cycling	Shirt pocket	30	3.5	37.4	52.0	72.3	10.4
	Waist belt	29	3.8	36.3	45.4	59.2	9.1
	Trouser pocket	30	1.1	35.6	41.3	59.5	8.3

unit's placement on the human body [16], [18]. We observed this in measurements that we conducted, especially for sensing units attached to the lower legs and lower arms. However, for the sensing unit placements examined in this section (shirt, waist, and trousers), the same motion resulted in similar f_m values, as can be seen in Fig. 5(b). These placements are on or near the torso, and are subjected to similar stresses. Cycling is an exception; the f_m for the trouser placement is different from the other placements. Because the body is in a sitting position, the stresses experienced by the legs and the torso are different and f_m differs for the different placements.

The uniformity of f_m offers valuable hints for energy harvesting node designers. People are likely to keep many objects that will become IoT nodes (keys, wallets, and cell phones) in pockets located in places that correspond to the placements we examine. This suggests that *a harvester tuned to a particular f_m will perform well regardless of where a person chooses to carry such an object.*

Inter-Participant Consistency: For common periodic motions, such as walking and running, the f_m values are relatively consistent among the different participants. The 25th and 75th percentiles of the participants' f_m values are separated by only 0.15 Hz for walking and by only 0.3 Hz for running. For less commonly practiced motions (cycling, going upstairs, going downstairs), the values of f_m are less consistent, but are still somewhat similar. This consistency indicates that *an all-purpose harvester designed for human walking or running will work reasonably well for a large number of different people.* The next section examines whether harvesters can be tuned to particular human parameters.

D. Dependency on Human Height and Weight

We examine the dependency of energy availability on human physiological parameters. We correlate D, f_m, and $\overline{P}$ obtained for different motions and different participants with their height and weight data from [20].[9] The participants' heights range was 155–182 cm, and their weights range was 44–65 kg. We verified that, in agreement with general human physiology studies, the

participants' height and weight are strongly positively correlated ($\rho = 0.7$, $p < 0.001$).

As indicated in the previous subsection, for many activities f_m is consistent among different participants. Yet, we additionally observed f_m dependencies on human physiology. For many of the activities we examined, we determined *negative correlations* of f_m *with the participants' height and weight.* When walking, running, and going upstairs and downstairs, heavier and taller people took fewer steps per time interval than lighter and shorter people.

For example, for going upstairs with waist unit placement, f_m and the participant's height are correlated as $\rho = -0.34$ ($p = 0.03$, $n = 39$). When going upstairs, the taller half of the participants made, on average, 9 fewer steps per minute (0.15 Hz) than the shorter half ($f_m = 1.85$ and 2.05 Hz, correspondingly). For running, with trouser placement, f_m and the participant's weight are correlated as $\rho = -0.46$ ($p < 0.01$, $n = 39$). When running, the heavier half of the participants made, on average, 18 fewer steps per minute (0.3 Hz) than the lighter half. This suggests that future harvester designs may benefit from targeting harvesters with different f_r values for human groups with different physiological parameters. For example, different harvesters may be integrated in clothing of different sizes.

Generally, motion energy availability increases as f_m increases [11]. However, in human motion, other dependencies may additionally come into play. In our study, for running with trouser unit placement, we determined a positive correlation between D and participants' height ($\rho = 0.35$, $p = 0.03$, $n = 38$) and a positive correlation between $\overline{P}$ and participants' height ($\rho = 0.38$, $p = 0.01$, $n = 38$). For the taller half of the participants, the average $\overline{P}$ is 20% higher than for the shorter half (704 and 582 μW, respectively). Studies with larger number of participants, wider participant demographics, and wider range of participant parameters will most likely identify many additional dependencies. This will allow harvester designers to *develop harvesters for different demographics*, as well as to provide guarantees on the performance of different harvesters based on different human parameters.

V. LONG-TERM HUMAN MOBILITY AND OBJECT MOTION ENERGY

The results presented in the previous section are based on short motion samples from an activity recognition dataset.

---

[9]The dataset [20] is also annotated with participants' age and gender. However, the age range (20 to 23 years) and the number of females (10 participants) are insufficient for obtaining statistically significant correlations.
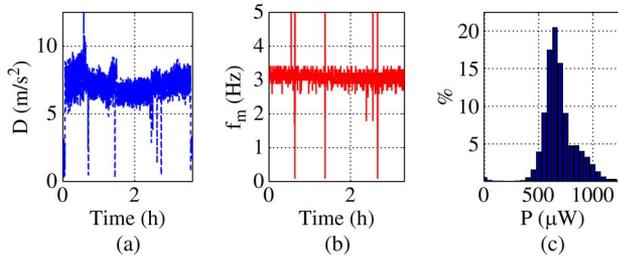
Fig. 6. Motion energy characterization for a 3 hour run: (a) the absolute deviation of acceleration, D, and (b) dominant motion frequency, f_m, as functions of time, and (c) the distribution of the corresponding power harvested, $P(t)$.

In this section, we present results of our own, *longer-term, motion measurements*. We describe our set of day-long human mobility measurements and discuss energy budgets and generation process properties. Specifically, we show that the energy generation cannot be modeled using a Markov process or by independent identically distributed (i.i.d.) random variables. Therefore, there is a need to revisit the design principles of energy-harvesting aware algorithms since many of them have been developed under the assumption of i.i.d. or Markov energy generation processes. Accordingly, there is a need to *develop algorithms that will take into account the special characteristics of the harvesting process*.

A. Prolonged Activities

To study motion energy properties over time, we collected a set of measurements of longer activity durations (over 20 minutes). We considered long walks, bike rides, runs, and other activities, performed in normal environments (i.e., not on a treadmill or a stationary bike). To the best of our knowledge, the properties of longer motion samples were not been analyzed before.

The measurements demonstrate that for prolonged activities, D, f_m, and $P(t)$ vary substantially over time. This variability is related to physiological parameters, such as changes in cadence or posture over time due to fatigue, and changes in the surrounding environment, such as traffic lights, terrain changes, or pedestrian traffic. For example, Fig. 6 shows D, f_m, and P corresponding to a 3 hour run, calculated for 1-second $a(t)$ intervals. In this trace, the average D changes subtly over time (Fig. 6(a)), and f_m varies continuously in the 2.6–3.4 Hz range (Fig. 6(b)). Correspondingly, while the mean $P(t)$ is 550 μW, the 10th–90th percentiles of the $P(t)$ span the range of 459–710 μW (Fig. 6(c)).

The variability of $P(t)$ throughout an activity suggests that node energy management policies are essential even for specifically targeted IoT applications, such as nodes for fitness runners or cyclists. In the following section we demonstrate even more variability in $P(t)$ for the regular everyday human mobility patterns.

B. Day-Long Human Mobility

To determine the daily energy available to an IoT node with an inertial harvester, we collected acceleration traces from different participants during their normal daily routines. We obtained over 200 hours of acceleration information for 5 participants for a total of 25 days (the traces are available in [21]). The participants (see Table III) were instructed to carry a sensing unit in any convenient way. Thus, the measurements correspond to the motion that a participant's keys, mobile phone, or wallet would experience.

Fig. 7 shows the $a(t)$ for a day-long trace of participant $M5$, and the corresponding $P(t)$. For all the collected traces, the dominant motion frequency, f_m, range is 1.92–2.8 Hz, corresponding to human walking.

The calculated energy budgets are summarized in Table III. We calculated $\overline{P}$, the average power a harvester would generate over the length of the trace, as well as $\overline{P_d}$, the average power a harvester would generate over a 24-hour interval. To calculate $\overline{P_d}$ we assumed that when the sensing unit did not record data (e.g., before the participants got dressed for school or work), it was stationary and that a harvester would not generate energy during these intervals. Specifically, for a T hour-long measurement trace, $\overline{P_d} = \overline{P} \cdot T / 24$. For each of the participants, Table III summarizes the minimum, average, and maximum $\overline{P}$ and $\overline{P_d}$ over the different measurement days, and the data rate r_d that a node would be able to maintain continuously throughout a day when powered by the harvested $\overline{P_d}$. For completeness, for all participants we additionally calculate $\overline{P}^{H4}$, the average power a particular harvester, same for all participants (in this case, the harvester calculated based on the traces for participant $M4$), would harvest. An extensive examination of the sensitivity of power harvested to different harvester design parameters is subject of ongoing work.

1) Power Budgets: For most participants, an inertial harvester can provide sufficient power to continuously maintain a data rate of at least 1 Kb/s (i.e., $\overline{P_d} > 5\mu$W). This is comparable with the data rates estimated in [13] for nodes with a similarly sized *light* harvester in indoor environments (not exposed to outdoor light).

The majority of inter-participant and inter-day differences seem to relate to the *participants' amount of walking*. For example, participant $M2$, whose $\overline{P}$ and $\overline{P_d}$ values are higher than the others, has a relatively long walk to the office, and walks frequently between two different offices in the same building. Other factors (unit placement, amount of daily activity as perceived by the participants) appear to be only of secondary importance. We note that the majority of traces that correspond to $\overline{P_d} < 5$ μW (and thus $r_d < 1$ Kb/s) correspond to participants *working from home*.[10] Overall, daily routines that involve a lot of walking correspond to relatively high levels of energy availability.

2) Harvesting Process Variability and Properties: The amount of energy that can be harvested varies widely throughout the day. As shown in Section IV, walking generates substantial amounts of energy, while being stationary generates little. Physiological studies (e.g., [30]) have shown that people are at rest the majority of the time. Correspondingly, in our measurements, $P(t)$ is low for most of the day and over 95% of the total energy is collected during only 4–7% of a day. For

---

[10]As indicated by the minimum value of $\overline{P_d}$ in Table III, several individual traces with $\overline{P_d} < 5$ μW were considered for participants M1, M3, and M4.

TABLE III
ENERGY BUDGETS, VARIABILITY, AND DATA RATES BASED ON COLLECTED TRACES FOR DAILY HUMAN ROUTINES

| Participant	Occupation and commute	# days	Total dur. (h)	Optimized harvester P (μW), min/avg/max	P_d (μW), min/avg/max	r_d, avg (Kb/s)	$\overline{P}^{H4}$ (μW), min/avg/max	% ON, min/avg/max
$M1$	Undergraduate student, male, living on campus, always goes to the lab	5	60.4	6.9 / 13.8 / 17.3	4.8 / 6.5 / 8.1	1.3	5.0 / 8.5 / 10.9	5.4 / 9.9 / 12.2
$M2$	Undergraduate student, male, commuting to campus, always goes to the lab	3	27.7	23.3 / 29.0 / 38.2	8.4 / 11.5 / 17.7	2.3	17.1 / 19.6 / 24.5	13.6 / 16.1 / 18.4
$M3$	Undergraduate student, female, living on campus, sometimes works from home	9	62.0	2.4 / 7.16 / 13.4	0.6 / 2.02 / 3.6	0.4	2.0 / 5.8 / 12.2	3.6 / 6.0 /9.95
$M4$	Graduate student, female, commuting to campus, sometimes works from home	7	80.1	1.4 / 11.98 / 25.3	0.6 / 5.6 / 10.7	1.1	1.4 / 11.98 / 25.3	2.8 / 12.7 / 18.1
$M5$	Software developer, male, commuting to office, always goes to the office	1	11.0	16.3	7.5	1.5	15.9	11.5
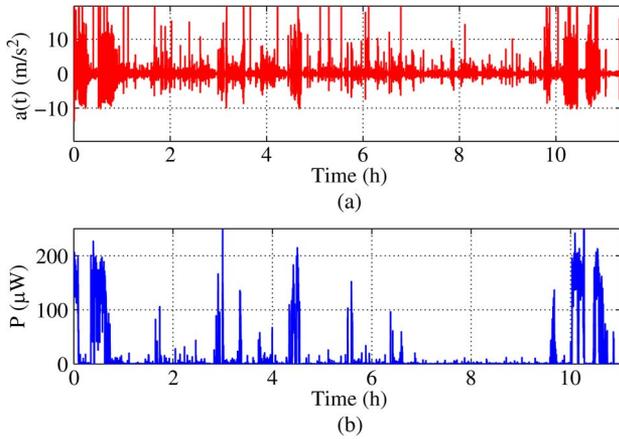
Fig. 7. Kinetic energy for normal daily human routine: (a) acceleration, $a(t)$, recorded over 11 hours for participant $M5$, and (b) the power harvested, $P(t)$.
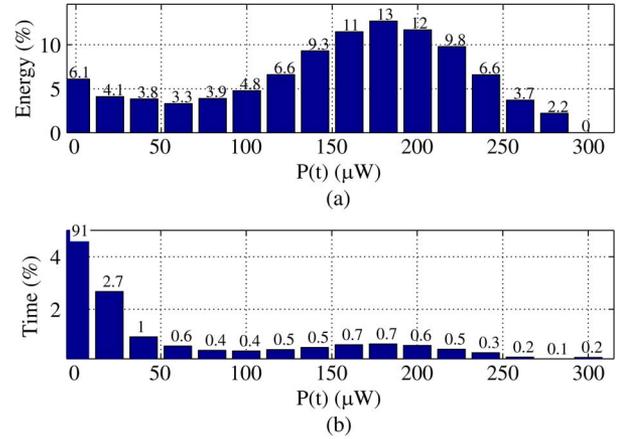

Fig. 8. Motion energy harvesting process variability for participant $M1$: (a) the percentage of the total energy harvested at different power levels $P(t)$, and (b) the *percentage of time* the power is harvested at the different $P(t)$ (notice that for $0 \le P(t) \le 15$, the value is 91%).

example, Fig. 8 shows, for participant $M1$, the percentage of the total energy that would be harvested over different ranges of $P(t)$ and the *percentage of the time* that the harvester would generate these $P(t)$ values. For this participant, the harvester would generate $P(t) < 15$ μW 91% of the time, and only 6.1% of the total energy would be harvested during this time.

Consider an *ON/OFF representation* of the energy harvesting process, $P_{\text{onoff}}(t)$, where $P_{\text{onoff}}(t) \leftarrow ON$ if $P(t) > \gamma$, and $P_{\text{onoff}}(t) \leftarrow OFF$ otherwise. For the analysis below, we empirically set $\gamma = 10$ μW; the results are similar for $10 \le \gamma \le 40$ μW. For all participants, P_{onoff} is ON for less than 20% of the time (Table III). The participants do not lead sedentary lifestyles; their activity patterns are in line with general health guidelines. However, the generally recommended 30 minutes of physical activity per day correspond to only 9% of an 11-hour trace. Additionally, the typical *duration* of ON intervals is short—*on the order of seconds*. While some of the ON intervals are long (over 200 seconds), the vast majority of the ON intervals (78.5–89.0%) are shorter than 30 seconds; the *median ON intervals are 5–9.5 seconds*. The longer ON intervals correspond to commuting (e.g., walking from a public transit station to a campus building), and represent only 1–3% of the ON intervals. These results are consistent with the overall results for

walking intervals examined in a physiological study of human mobility [30].

In summary, $P(t)$ is low for the majority of the time, and when it does become high, it stays high for only a brief period of time. This emphasizes the need for energy harvesting-adaptive algorithms.

3) Harvesting Process vs. I.i.d. and Markov Processes: Several energy harvesting adaptive algorithms were developed under the assumption that the energy harvesting process is Markov, or has independent identically distributed (i.i.d.) per-slot energy inputs [13], [15], [42]. However, such assumptions, realistic in certain scenarios [13], *do not hold for our motion energy traces*. We use a slotted representation of the energy harvesting processes, P_{meas}, setting the time slot length $T_{\text{int}} = 1$ second, and determining the $P_{\text{meas}}(i)$ by computing the average value of the $P(t)$ for each T_{int}. For all day-long traces, P_{meas} is *clearly not i.i.d. or Markovian*. For example, for the P_{meas} for participant $M1$ for $\gamma = 20$ μW, $p(P_{\text{meas}}(i) > \gamma | P_{\text{meas}}(i-1) > \gamma) = 0.84$, while $p(P_{\text{meas}}(i) > \gamma | P_{\text{meas}}(i-1) > \gamma, P_{\text{meas}}(i-2) < \gamma) = 0.45$.

To demonstrate the differences between the traces and i.i.d. and Markov processes, we examine the performance of the
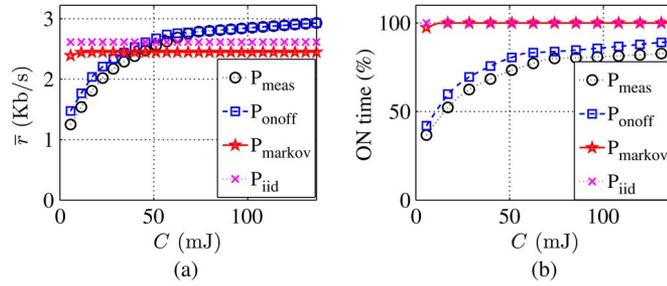
Fig. 9. Scheme-LB policy performance using energy traces (P_{meas}) for participant $M1$ and using the corresponding ON/OFF (P_{onoff}), Markov (P_{Markov}), and i.i.d. (P_{iid}) processes: (a) average data rates, $\bar{r}$, and (b) node ON times.

TABLE IV
OBJECT MOTION MEASUREMENTS

Scenario	$\bar{P}$
Taking a book off a shelf	<10 μW
Putting on reading glasses	<10 μW
Reading a book	<10 μW
Writing with a pencil	10–15 μW
Opening a drawer	10–30 μW
Spinning in a swivel chair	<10 μW
Opening a building door	<1 μW
Shaking an object	>3,000 μW

Scheme-LB policies [12] with the different processes. In the Scheme-LB policies [12], $s(i) \leftarrow (1-\varepsilon)\hat{Q}(i)$ if $B(i) + Q(i) \geq (1-\varepsilon)\hat{Q}(i)$, and $s(i) \leftarrow B(i) + Q(i)$ otherwise, where $\hat{Q}(i)$ is the running average of $Q(i) (\hat{Q}(i) \leftarrow \sum_{j=0}^{i-1} Q(j)/i)$, and ε is a small constant (we use $\varepsilon = 0.01$). For a process P_{meas}, we generate a corresponding i.i.d. process, P_{iid}, by randomly permuting the values of P_{meas} (we use the Wald-Wolfowitz runs test to verify the independence of the P_{iid} values). To generate a Markov process, P_{Markov}, we calculate the empirical state transition probabilities of the P_{onoff} process (defined in Section V-B2) and generate a Markov process with states {ON, OFF} and the calculated transition probabilities. We set the P_{Markov} values for ON and OFF states to the average values of $P_{\text{meas}}(i)$ for which $P_{\text{onoff}}(i) = ON$, and for which $P_{\text{onoff}}(i) = OFF$, respectively. This ensures that *the processes have the same first-order statistics*.[11]

The policy performance observed using i.i.d. and Markov processes differs dramatically from the policy performance observed using the traces. For example, Fig. 9 shows the $\bar{r}$ and the ON times obtained under the Scheme-LB policy for the different processes based on a trace of participant $M1$. Using the process P_{onoff}, the performance is similar to the performance obtained using P_{meas}—the $\bar{r}$ values differ by at most 17% (0.23 Kb/s), and the ON times differ by at most 7%. However, the performance observed using P_{iid} and P_{Markov} differs greatly from the performance observed using P_{meas}. The differences in $\bar{r}$ values reach over 105% (1.35 Kb/s), and the differences in ON times reach 63%.

Moreover, using i.i.d. and Markov processes results in *different performance trends*. Using P_{meas}, the performance strongly depends on C, with $\bar{r}$ for the different values of C differing by over 2.3 times, and with the ON percentages differing by over 45%. However, using P_{iid} and P_{Markov}, both $\bar{r}$ and ON times are nearly independent of C. Additionally, evaluating policy performance using P_{meas} shows that the ON times are an important metric because they can be low for small values of C (Fig. 9(b)). However, when evaluating using P_{iid} and P_{Markov}, the ON times are nearly 100% for all values of C, including values as low as 15 mJ (i.e., less than 15% of the average energy harvested per day). This *emphasizes the need to evaluate energy*

harvesting-adaptive policies for wireless nodes equipped with an inertial harvester using real traces.

C. Object Motion Energy

While Sections IV and V focus on *human motion*, in this section we also provide some brief observations regarding the energy availability associated with the *motion of objects*. This study is motivated by various IoT applications, including inventory management and object tracking, which require attaching small devices to everyday objects (e.g., keys, books, packages). We conducted extensive experiments, recording $a(t)$ and calculating $\bar{P}$ for a wide range of motions. Our experiments included performing everyday activities with a variety of everyday objects (see Table IV), shipping a FedEx box with a sensing unit in it from Houston, TX to New York, NY, transporting sensing units in carry-on and checked airport luggage, and taking sensing units on cars, subways, and trains. Below, we present observations based on our measurements. To put the $\bar{P}$ values in perspective, we note that, as we demonstrated in Section IV, *human walking* typically corresponds to $120 \leq \bar{P} \leq 280 \, \mu$W.

Expectedly, for the vast majority of common object motion the energy availability is low. Due to the filter properties of inertial harvesters (see Section III-A), a motion needs to be *periodic* to be "harvestable". The vast majority of common object motion is not periodic, and hence the corresponding energy availability is low. For example, we attached a sensing unit to a book and observed that when the book is being taken off the shelf, read, or put back on the shelf, $\bar{P} < 10 \, \mu$W. For a sensing unit attached to a pencil used by a student to write homework, $10 \leq \bar{P} \leq 15 \, \mu$W. Even high-acceleration non-periodic motions, such as a plane landing and taking off, and an accelerating or decelerating car, correspond to only limited energy availability ($\bar{P} < 5 \, \mu$W. For example, when a unit was placed in a bag checked in on a $3:13$ hour flight the recorded $a(t)$ showed that the luggage was subjected to varying high-acceleration motions, but the $\bar{P}$ did not exceed 5 μW even during the most turbulent intervals of the flight. Furthermore, substantially more energy could be harvested from a human walking around the airport with the luggage (i.e., periodic motion of a human walk) than from the motion associated with the entire flight.

Our study additionally demonstrated low levels of energy availability for many *high-amplitude and high-periodicity* motions. The motion of many objects in our environment is *damped* for human comfort (e.g., by door dampers, cabinet drawer dampers, and springs in swirling chairs). In such cases, most of the motion energy is absorbed in the dampers and only small amounts can be harvested (e.g., by sticker form factor

---

[11]For each of the processes, we calculate $Q(i)$ as $Q(i) \leftarrow \eta_h \cdot T_{\text{int}} \cdot P(i)$, where $\eta_h = 20\%$ [16]. We rely on a *battery* node model and set $B_0 = 0.5C$. We calculate the data rate as $r(i) \leftarrow s(i)/c_{\text{tx}}$.

harvesters [3]). Opening and closing a drawer, spinning a swivel chair, and opening and closing a building door corresponded to $10 \leq \overline{P} \leq 30\,\mu$W, $1 \leq \overline{P} \leq 6.5\,\mu$W, and $\overline{P} < 1\,\mu$W, respectively. This suggest that IoT nodes embedded in objects such as doors and drawers should *integrate motion energy harvesters with the mechanical dampers*.

Finally, our study confirmed that purposeful object motion can be extremely energy rich. Periodic shaking of objects can generate a relatively large amount of energy in a short time (as demonstrated by "shake" flashlights). In our experiments, purposeful shaking corresponded to $\overline{P}$ of up to 3,500 μW, that is, *12–29 times more than the power for walking*. In IoT applications with mobile nodes, this can be useful for quickly recharging battery-depleted nodes.

VI. ENERGY-AWARE ALGORITHMS

We now formulate an optimization problem of energy allocation for ultra-low-power energy harvesting IoT node and prove it to be NP-hard. As mentioned in Section III-E, the formulation captures realistic constraints that have not been jointly considered before: (i) *discrete*, rather than continuous, energy spending rates; (ii) *general*, rather than concave or linear, utility functions; and (iii) use of a *capacitor*, rather than a battery, as an energy storage component.

In Section V-B3 we demonstrated that the environmental energy available to the node in each slot i, $e(i)$, cannot be represented by a Markov or an i.i.d. process. Therefore, there is need to develop algorithms that do not make an assumption on the distribution of $e(i)$. Since the energy allocation problem is NP-hard, solving it is difficult even if $e(i)\ \forall i$ is known in advance. We distinguish between two types of energy allocation algorithms: (i) *offline*, where $e(i)\ \forall i$ is part of the input; an offline algorithm can be used as a benchmark since it provides an upper bound on the utility a node can achieve in practice, and (ii) *online*, where a decision in slot i is made based only on $e(i')\ \forall i' < i$; an online algorithm can be used by a real node to determine spending rate $s(i)$ in each slot. We develop optimal and approximate offline algorithms. We then develop an online algorithm and prove it to be optimal for some cases. We also evaluate the performance of the algorithms with the collected motion energy traces. The proofs for this section appear in Appendix I.

A. Energy Allocation Problem

We start by formulating the energy allocation problem for a wireless IoT node:

Energy Allocation (EA) Problem:

$$\max_{s(i)} \left\{ \sum_{i=0}^{K-1} U\left(s(i)\right) \right\} \text{ s.t. :}$$

$$\frac{s(i)}{\eta\left(i,B(i)\right)} \leq B(i),\ s(i) \in \mathcal{S} \cup \{0\}\ \forall\, i \qquad (1)$$

$$B(i) \leq B(i-1) + Q\left(e(i-1),B(i-1)\right)$$

$$-L(i-1,B(i-1)) - \frac{s(i-1)}{\eta\left(i-1,B(i-1)\right)}\ \forall\, i \geq 1 \qquad (2)$$

$$0 \leq B(i) \leq C\ \forall\, i;\ B(0) = B_0; B(K) \geq B_K \qquad (3)$$

This is an integer optimization problem, namely, all the coefficients and function values are integers. Constraint (1) ensures that a node does not spend more energy than it has stored and that the spending rate, $s(i)$, is from a fixed set, (2) represents the energy storage evolution dynamics, and (3) imposes the storage component capacity constraints and sets the initial and final energy levels to B_0 and B_K. To simplify the notation, we omit the dependency of $\eta(i,B(i))$, $Q(e(i),B(i))$, and $L(i,B(i))$, on $B(i)$ in the rest of the section. However, unless mentioned otherwise, the proofs and the algorithms are also valid when the dependency on $B(i)$ is considered.

The proof of the following theorem demonstrates the NP-hardness of the EA Problem even for "simple" cases (e.g., $B_0 = B_K = 0$ and linear $U(s(i))$).

Theorem 1: The EA Problem is NP-hard.

B. Energy Allocation Algorithms

For solving the EA Problem, we present a dynamic programming-based pseudopolynomial algorithm,[12] a Fully P-olynomial Time Approximation Scheme (FPTAS),[13] and a greedy online algorithm which is optimal in particular scenarios.

We first present an optimal offline dynamic programming algorithm for solving the EA Problem. Thus, the algorithm jointly considers realistic constraints that have not been jointly considered before and uses similar ideas to the dynamic programming algorithm from [13]. However, compared to [13], the dynamic programming procedure's parameters and return value switch places. This difference is used to develop the FPTAS we present later in this section.

Dynamic Programming Algorithm: We determine $M(i,U)$ which is the maximum battery level when obtaining utility U in the beginning of slot i. We set $M(0,0) = B_0$ and $M(0,U) = -\infty\ \forall\ U > 0$. For $i > 0$, $M(i,U)$ is calculated as $M(i,U) = \max_{s(i-1)\in\mathcal{S}\cup\{0\}}\{M(i-1,U - U(s(i-1))) + Q(i-1) - s(i-1)/\eta(i-1) - L(i-1)\}$. Let the optimal solution utility be U^*, and let $U^H \geq U^*$ be an upper bound. We calculate $M(i,U)$ for $1 \leq i \leq K$ and $0 \leq U \leq U^H$. Then, $U^* = \arg\max\{M(K,U)$ s.t. $M(K,U) \geq B_K\}$. The optimal energy spending values $s^*(i)$ are found by maintaining an array $A(i,U)$ that stores the $s(i-1)$ values chosen when calculating $M(i,U)$. Then, $s^*(K-1) = A(K,U^*)$. We can obtain $s(K-2)$ using $A(K-1,U^* - U(s^*(K-1)))$. This process is repeated to find $s^*(i)$ for $0 \leq i \leq K-1$.

The space complexity of the algorithm is $O(K \cdot U^H)$ for storing $A(i,U)$. Since in every calculation of $M(i,U)$ we go over $\mathcal{S}$, the time complexity is $O(K \cdot |\mathcal{S}| \cdot U^H)$. Let $s_{\max}$ be the maximum item in $\mathcal{S}$, clearly $U^H = K \cdot U(s_{\max})$ is an upper bound, for which we obtain space and time complexities of $O(K^2 \cdot U(s_{\max}))$ and $O(K^2 \cdot U(s_{\max}) \cdot |\mathcal{S}|)$, respectively.

FPTAS: For large values of $U(s_{\max})$, the time and space complexities render the dynamic programming algorithm im-

---

[12]A *pseudopolynomial algorithm* is an algorithm whose running time is polynomial if the input is encoded in unary format.

[13]An *FPTAS* is an algorithm which takes an instance of an optimization problem and a parameter $\varepsilon > 0$ and, in polynomial time in both the problem size and $1/\varepsilon$, produces a solution that is within a $1-\varepsilon$ factor of the optimal solution.

practical. Therefore, we develop an approximation scheme. It relies on a lower bound $U^L = U(s_{max})$, which is a lower bound, since if spending only s_{max} energy at some slot is always infeasible, s_{max} can be removed from $\mathcal{S}$. We define a scaling factor $\mu = \varepsilon \cdot U(s_{max})/K$ and a new utility function $\tilde{U}(s) = \lfloor U(s)/\mu \rfloor$. Next, we invoke the dynamic programming algorithm for $\tilde{U}()$ to compute $M(i, \tilde{U})$ for $0 \leq i \leq K$ and $0 \leq \tilde{U} \leq U^H/\mu$. The algorithm returns the energy spending rates $\tilde{s}(i)$ found by the dynamic programming algorithm. Below we show that the algorithm is an FPTAS.

Theorem 2: The above algorithm runs in times $\text{poly}(1/\varepsilon, K)$, and the solution $\tilde{s}(i)$ is a $(1-\varepsilon)$-approximation.

Greedy Online Algorithm: In every time slot, the algorithm tries to maximize the utility while not letting the energy storage level go below B_K. Namely, in each slot i the algorithm spends $s(i) = \max\{U(s) \mid s \in \mathcal{S} \cup \{0\} \wedge (B(i) - s/\eta) \geq B_K\}$.

We first focus on the *battery* node model and on a scenario where (i) for x, y, $U(x+y) = U(x) + U(y)$, and (ii) the set $\mathcal{S}$ is $\{j \cdot s, j = 1, \ldots, |\mathcal{S}|\}$ and $s > 0$. Such conditions hold, for example, when a node uses a fixed power level and changes its transmission rate by transmitting a different number of equal-sized packets.

Theorem 3: For battery energy storage model, for $B_K = 0$, if conditions (i) and (ii) hold, the greedy algorithm is optimal.

In Section VI-C we evaluate the performance of the greedy online algorithm under the capacitor model and for cases where $B_K > 0$.

To complement Theorem 3, Theorem 4 below shows that for cases where $B_K > 0$, any online algorithm performs arbitrary bad. Since we showed in Section V-B3 that $e(i)$ cannot be represented by a Markov or an i.i.d process, for these cases any online algorithm may perform arbitrary worse and it should be evaluated with collected traces to assess its performance.

Theorem 4: For $B_K > 0$, the performance of any online algorithm that guarantees a feasible solution can be arbitrary bad for $K \geq 2$.

C. Trace-Based Performance Evaluation

In this section, we evaluate the algorithms using the motion energy traces we collected, for both *battery* and *capacitor* node models defined in Section III-E. We refer to the algorithm and model combinations as follows:

Algorithms Invoked for the Battery Model:
- **ALG-OB**: The optimal dynamic programming algorithm.
- **ALG-FB**: The FPTAS.
- **ALG-GB**: The greedy online algorithm.

Algorithms Invoked for the Capacitor Model:
- **ALG-OC**: The optimal dynamic programming algorithm.
- **ALG-FC**: The FPTAS.
- **ALG-GC**: The greedy online algorithm.

We consider an IoT node that changes its data rate $r(i)$ by changing the number of packets it sends in a time slot (where the length of a time slot is $T_{int} = 1$ second). The maximal $r(i)$ is 250 Kb/s, the packet size is 127 bytes,[14] and $c_{tx} = 1$ nJ/bit (i.e.,
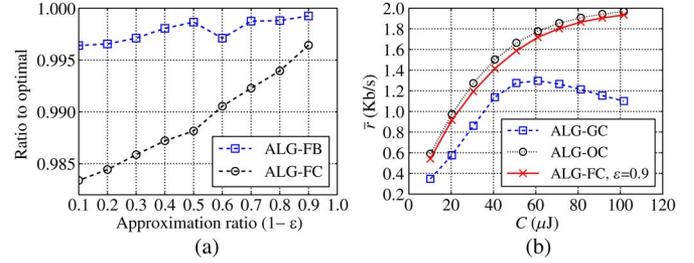

Fig. 10. Algorithm performance using energy traces for participant $M1$, for: (a) battery and capacitor models, performance ratio between ALG-FC (ALG-FB) and ALG-OC (ALG-OB), and (b) the capacitor model, average data rate, $\bar{r}$, achieved by different algorithms.

it takes 1,016 nJ to transmit 1 packet). Thus, $\mathcal{S} = \{1016 \cdot j, j = 1, \ldots, 246\}$, and $s_{min} = \min\{s \in \mathcal{S}\} = 1016$. We set $L(i, B(i)) = 0$. We use the day-long motion energy traces (see Table III).[15] We evaluated the algorithms for traces of different users and for different days. We observed that the performance trends of the algorithms are very similar for all the considered day-long traces. Therefore, only the graphs corresponding to a day-long trace of participant $M1$ are shown. Since for the day-long traces K is very large, to draw a single point in the graphs we run the algorithms over 66 consecutive 10-minute intervals of $Q(i)$ and average the results. Unless specified otherwise, the evaluation results are shown for $B_0 = B_K = 0$ and for $10 \cdot s_{min} \leq C \leq 100 \cdot s_{min}$.

We first explain in detail how to compute the conversion efficiency $\eta()$. Recall that $\eta()$ depends on the node's fixed operating voltage V_{op} and energy storage voltage $V_{out}(i)$ (see Section III-E). For the *battery* model, we assume $V_{out}(i) = V_{op}$ and set $\eta = 1$. For the *capacitor* model, approximating voltage converter properties [44], we compute:

$$\eta(i, B(i)) = \begin{cases} \frac{V_{out}(i)}{V_{op}}, & V_{min} \leq V_{out}(i) \leq V_{op} \\ 1 - \frac{V_{out}(i) - V_{op}}{2 \cdot (V_{max} - V_{op})}, & V_{op} < V_{out}(i) \leq V_{max} \\ 0 & \text{otherwise} \end{cases}$$

where $V_{max} = 2.8$ V is the maximum voltage of the capacitor, $V_{out}(i)$ is node's voltage in a time slot $i(V_{out}(i) = \sqrt{B(i)/C} \cdot V_{max})$, $V_{op} = 2.5$ V, and $V_{min} = 0.7$ V.

We first examine the performance of ALG-FC as a function of its approximation ratio, $1 - \varepsilon$ (see Theorem 2). Fig. 10(a) shows the ratio of the ALG-FC performance to the optimal (ALG-OC) for $C = 100 \cdot s_{min}$. Even for small $1 - \varepsilon$, the ALG-FC performance is close to the optimal (much closer than the theoretical bound). Similar results were obtained for ALG-FB.

Next, we examine the performance of the ALG-GC, ALG-OC, and ALG-FC for the capacitor mode. Fig. 10(b) shows the average data rates $\bar{r}$ obtained by the algorithms. The performance of ALG-FC is close to that of ALG-OC. The performance of ALG-GC gets worse compared to ALG-OC for larger C because it obtains lower $V_{out}(i)$ (recall that $V_{out}(i) = \sqrt{B(i)/C} \cdot V_{max}$), resulting in lower $\eta()$. Furthermore, for $C > 60 \mu J$, its obtained $\bar{r}$ *decreases* as C increases.

---

[14]These parameters correspond to IEEE 802.15.4/Zigbee nodes [43].

[15]From the traces, we calculate $Q(i)$ as $Q(i) \leftarrow \eta_h \cdot T_{int} \cdot P_{meas}(i)$, where $\eta_h = 20\%$. To evaluate ALG-GB, ALG-FC, and ALG-GC, we compare their performance with the optimal algorithms ALG-OC and ALG-OB.
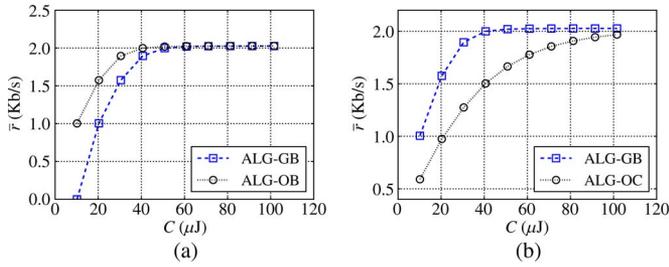
Fig. 11. The average data rate, $\bar{r}$, achieved by the algorithms using energy traces for participant $M1$, for (a) the battery model, for $B_K = B_0 = 10 \cdot s_{\min}$, and (b) the battery and capacitor models.
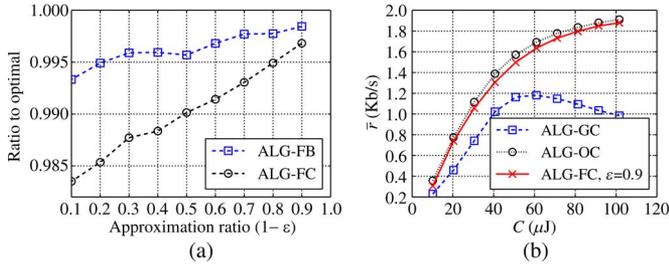

Fig. 12. Algorithm performance using energy traces for participant $M1$, for: (a) battery and capacitor models, performance ratio between ALG-FC (ALG-FB) and ALG-OC (ALG-OB), and (b) the capacitor model, average data rate, $\bar{r}$, achieved by different algorithms.
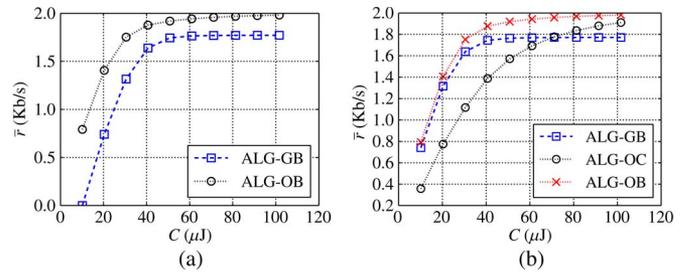

Fig. 13. The average data rate, $\bar{r}$, achieved by the algorithms using energy traces for participant $M1$, for (a) the battery model, for $B_K = B_0 = 10 \cdot s_{\min}$, and (b) the battery and capacitor models.
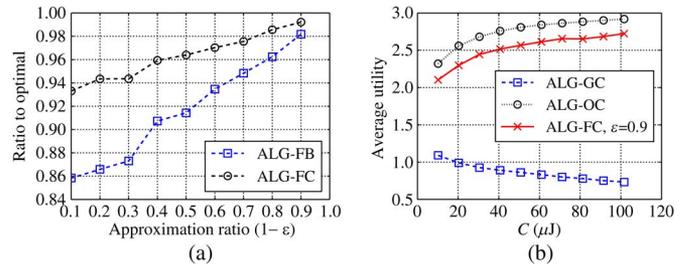

Fig. 14. Algorithm performance using energy traces for participant $M1$ and and considering a sensing device, for: (a) battery and capacitor models, performance ratio between ALG-FC (ALG-FB) and ALG-OC (ALG-OB), and (b) the capacitor model, average data rate, $\bar{r}$, achieved by different algorithms.
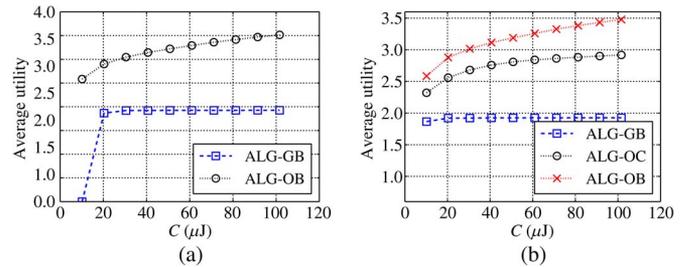

Fig. 15. The average utility, achieved by the algorithms using energy traces for participant $M1$, where the utility corresponds to the channel capacity, for (a) the battery model, for $B_K = B_0 = 10 \cdot s_{\min}$, and (b) the battery and capacitor models.

We also examine the performance of the ALG-GB and ALG-OB algorithms for the battery model. Since for $B_K = 0$ ALG-GB is optimal (see Theorem 3), we consider $B_K = B_0 = 10 \cdot s_{\min}$. Fig. 11(a) shows the $\bar{r}$ values obtained by ALG-GB and ALG-OB. Since ALG-GB cannot take advantage of the initial energy (because $B_0 = B_K$), for a particular C value the capacity available to ALG-GB is $C - B_0$. Correspondingly, since consecutive plotted points differ by B_0 in their C value, the plotted points $(C, \bar{r})$ for ALG-OB and $(C + B_0, \bar{r})$ for ALG-GB appear in the figure.

To compare the performance for the battery and the capacitor models, Fig. 11(b) shows the data rates obtained by ALG-GB and ALG-OC. For ALG-OC, for larger C there is a wider range of charge level for which $\eta()$ is close to 1. Correspondingly, ALG-OC can keep $\eta()$ close to 1, thus its performance approaches that of ALG-GB.

Next, we consider the case where the node has a sensing device (e.g., temperature and humidity sensor [45]). Based on the parameters from [45], the sensor consumes 1,900 nJ per sensor measurement. Accordingly, we update S as $S = \{1016 \cdot j + 1900, j = 1, \ldots, 246\}$; note that Theorem 3 does not apply to this case. Figs. 12 and 13 illustrate numerical results obtained by the algorithms under these assumptions.

Fig. 12 demonstrates the same observations as those demonstrated in Fig. 10. Fig. 13(a) shows the $\bar{r}$ values obtained by ALG-GB and ALG-OB. Here ALG-GB does not reach the optimal solution (ALG-OB) even for large capacity values. This is because ALG-GB spends the energy as soon as it is available, resulting in more energy spent for sensing (instead using it for transmission). Fig. 13(b) shows the data rates obtained by ALG-OB, ALG-GB, and ALG-OC. We observe similar trends as in Fig. 11(b), except that ALG-GB is not optimal even for large capacity values. For large capacity values (over 70 μJ), ALG-

OC performs better than ALG-GB since ALG-OC can keep the capacitor level such that η is very close to 1.

Finally, we evaluate our algorithm for the case in which $U(s) = 0.5 \log(1 + s)$, where $U(s)$ corresponds to the channel capacity [46]. We use $S = \{1016 \cdot j, j = 1, \ldots, 246\}$.

Fig. 14(a) demonstrates that our FPTAS obtains much better performance ratio than the theoretical guarantee of $1 - \varepsilon$. In Fig. 14(b), we see that ALG-GC performs poorly in this case. In particular, as the capacity increases the performance of ALG-GC decreases. This is due to two reasons: (i) as before, for the capacitor model, larger capacity reduces η; and (ii) the usage of a concave $U(s)$ reduces the benefit from larger capacity.

Fig. 15(a) demonstrates that ALG-GB performs substantially worse than ALG-OB (55% performance ratio for high capacity values). The reason is, again, due to the concave nature of $U(s)$, which implies that small portions of energy spending over many slots is preferable. Fig. 15(b) demonstrates that, as expected, ALG-OB obtains the highest performance, followed by ALG-OC which loses some performance due to the conversion efficiency η. ALG-GB performs the worst in Fig. 15(b)

due to the concave utility function $U(s)$ and the non-optimality of ALG-GB.

In summary, the evaluations demonstrate that the algorithms perform well and showcase that for the *capacitor* node model, having a larger energy storage may worsen the overall performance.

VII. CONCLUSION

This paper considers motion (kinetic) energy availability for Internet of Things (IoT) applications. We thoroughly study *human motion* and provide observations regarding *object motion*. For human motion, we use the results of our measurement campaign that include 200 hours of acceleration traces from day-long human activities. Moreover, we use a dataset of 7 common human motions performed by over 40 participants [20]. We consider a wireless energy harvesting node model that captures several practical IoT node design considerations. We design optimal, approximation, and online *energy allocation algorithms* and evaluate their performance using the collected motion energy traces.

In future work we will expand our measurement study to include additional motions and additional human participants. Expanding the study for additional motions is motivated by the appearance of new wearable devices targeting specific activities (e.g., dancing, jumping). We will jointly measure light and motion energy (available to the same device) to obtain insight into the use of multipurpose harvesters.

APPENDIX I

Proof of Theorem 1: We prove that the EA Problem is NP-hard using a reduction from a well-known NP-hard problem [47]. The reduction performs several transformations, all of which are polynomial in time and space. We start with two definitions:

Definition 1: An instance of the EA Problem is defined using the integers $K \geq 0$, $C \geq 0$, $B_0 \geq 0$, and $B_K \geq 0$, the set $\mathcal{S}$, the functions $Q()$, $\eta()$, $U()$, and $L()$, and the value of $e(i)$ for every slot $i = 0, \ldots, K-1$.

Definition 2: Given an instance of the EA Problem, a vector $s(i)$, $i = 0, \ldots, K-1$ is feasible if constraints (1)–(3) hold with respect to it.

The *decision version* of the EA Problem (EA-D) is defined using the same values as those defining the EA Problem, as well as an additional integer $U \geq 0$. A solution to the EA-D Problem is a "yes" or "no" answer, where "yes" is returned if and only if there is a feasible vector $s(i)$ with $\sum_{i=0}^{K-1} U(s(i)) \geq U$. It is easy to see that given a polynomial-time solver to EA-D, one can solve the EA Problem using binary search on the values of U. Therefore, to prove that the EA Problem is NP-hard,

We show a polynomial time reduction from the decision form of subset sum Problem (SSP-D), which is known to be an NP-hard Problem [47]. The SSP-D Problem is defined as follows:

$$\text{SSP-D}(w,c) = \begin{cases} \exists x & \text{such that:} \\ \sum_{j=1}^{n} w_j x_j = c; & x_j \in \{0,1\} \ \forall j, \end{cases}$$

where $w = (w_1, \ldots, w_n)$ is a vector of size n. We assume that c and all coefficients w_j are integers.

It is clear that in any solution to SSP-D, the inequality $\sum_{j=1}^{n} x_j \leq n$ holds. Therefore, we can add this as an additional constraint to SSP-D. We also introduce slack variables y_j and obtain the following formulation equivalent to SSP-D, denoted SSP-D$_1$:

$$\text{SSP-D}_1(w,c) = \begin{cases} \exists x & \text{such that:} \\ \sum_{j=1}^{n} w_j x_j = c, & \sum_{j=1}^{n} x_j + y_j \leq n \\ x_j + y_j = 1, & x_j, y_j \in \mathbb{N}_0 \ \forall j. \end{cases}$$

We now follow the same technique as used in [47] to merge the equation $x_1 + y_1 = 1$ with the equation $\sum_{j=1}^{n} w_j x_j = c$, obtaining the new equation $x_1 + y_1 + 2\sum_{j=1}^{n} w_j x_j = 2c + 1$. As shown in [47], this does not change the set of feasible solutions. Repeating the process of merging with $x_j + y_j = 1$ for $j = 2, \ldots, n$, we get the following formulation, denoted SSP-D$_2$:

$$\text{SSP} - \text{D}_2(w,c) = \begin{cases} \exists x, y & \text{such that:} \\ 2^n \sum_{j=1}^{n} 2^{-j}(y_j + x_j) + \\ w_j x_j = 2^n c + 2^n - 1 \\ \sum_{j=1}^{n} x_j + y_j \leq n; & x_j, y_j \in \mathbb{N}_0 \ \forall j. \end{cases}$$

Setting $\tilde{w}_j = 2^{n-j} + 2^n w_j$, $\overline{w}_j = 2^{n-j}$, and $\overline{c} = 2^n c + 2^n - 1$, we reach the equivalent formulation, denoted SSP-D$_3$:

$$\text{SSP-D}_3(\tilde{w}, \overline{w}, c) = \begin{cases} \exists x, y & \text{such that:} \\ \sum_{j=1}^{n} \tilde{w}_j x_j + \overline{w}_j y_j = \overline{c}, \\ \sum_{j=1}^{n} x_j + y_j \leq n; & x_j, y_j \in \mathbb{N}_0 \forall j. \end{cases}$$

Let $n_b(w,c)$ be the number of bits required to represent (w,c). It is shown in [47] that the new coefficients $\tilde{w}_j$, $\overline{w}_j$, and $\overline{c}$, are polynomial in $n_b(w,c)$. Therefore, the transformation can be performed in polynomial time.

We now show how to reduce SSP-D$_3$ into an instance of EA-D, which will complete the proof. As input for EA-D we set $B_0 = B_K = 0$, $K = n+1$, $C = U = e(0) = \overline{c}$, $\mathcal{S} = \{\tilde{w}_j\} \cup \{\overline{w}_j\}$; $L(i) = 0$, $\eta(i) = 1 \forall i$; and $e(i) = 0 \forall i \geq 1$. We set $U()$ and $Q()$ as the identity function: $U(x) = x$ and $Q(x) = x$. Clearly, generating this input can be performed in polynomial time.

We now show that the reduction holds, namely, that the generated EA-D is a "yes" instance if and only if SSP-D$_3$ is a "yes" instance. Note that since $B_0 = 0$, we get $s(0) = 0$. In addition, $\forall i \geq 1$ $Q(i) = 0$, $B(1) = e(0) = \overline{c}$, and $B_K = 0$. Therefore, the considered EA-D instance is a "yes" instance if and only if there exist $s(i)$ such that $\sum_{i=1}^{n} s(i) \leq \overline{c}$ and $\sum_{i=1}^{n} U(s(i)) = \sum_{i=1}^{n} s(i) = \overline{c}$.

If the SSP-D$_3$ is a "yes" instance, there exist x_j, y_j such that $\sum_{j=1}^{n} x_j + y_j \leq n$. A feasible vector $s(i)$ for EA-D can be obtained as follows: for $j = 1, \ldots, n$, use x_j slots by spending $\tilde{w}_j$ amount of energy in each such slot and use y_j slots by spending $\overline{w}_j$ amount of energy in each such slot. Clearly, such energy spending is feasible and obtains the total utility of $U = \overline{c}$. Therefore, the EA-D is a "yes" instance. The other direction, namely, that if the EA-D instance is a "yes" instance, the SSP-D$_3$ instance is a "yes" instance, can be proved in a similar way. $\square$

Proof of Theorem 2: The total profit of the solution returned by the algorithm is $\sum_{\tilde{s}(i)} U(\tilde{s}(i))$, and, due to the definition of $\tilde{U}()$:

$$\sum_{i=0}^{K-1} U(\tilde{s}(i)) \geq \sum_{i=0}^{K-1} \mu \cdot \tilde{U}(\tilde{s}(i)).$$

Since the dynamic programming returns the optimal solution with respect to $\tilde{U}()$,

$$\mu \sum_{i=0}^{K-1} \tilde{U}(\tilde{s}(i)) \geq \mu \sum_{i=0}^{K-1} \tilde{U}(s^*(i)) \geq \sum_{i=0}^{K-1} \mu \left(\frac{U(s^*(i))}{\mu} - 1 \right)$$

$$\sum_{i=0}^{K-1} \mu \cdot \left(\frac{U(s^*(i))}{\mu} - 1 \right) \geq U^* - K \cdot \mu$$

Since $\mu = \frac{\varepsilon \cdot U(s_{\max})}{K}$ and $U^L = U(s_{\max})$, using the above equations, we get $\sum_{i=0}^{K-1} U(\tilde{s}(i)) \geq (1-\varepsilon)U^*$, which proves the approximation ratio.

Due to the invocations the dynamic programming with utility function $\tilde{U}()$, the space and time complexities are $O(K^2 \cdot \tilde{U}(s_{\max}))$ and $O(|\mathcal{S}| \cdot K^2 \cdot \tilde{U}(s_{\max}))$, respectively. Replacing $\tilde{U}(s_{\max})$ with $\frac{U(s_{\max})}{\mu}$, we obtain the space and time complexities of $O(\frac{K^3}{\varepsilon})$ and $O(|\mathcal{S}| \cdot \frac{K^3}{\varepsilon})$, respectively. $\square$

Proof of Theorem 3: We first make the following observation [29], [40]:

Observation 1: Let i_1 and i_2 be two slots. If $B(i_1) \geq B(i_2)$, then $L(i_1) \geq L(i_2)$.

Since condition (i) holds, $\sum_{i=0}^{K-1} U(s(i)) = U(\sum_{i=0}^{K-1} s(i))$ and the total energy spent is $\eta_h \sum_{i=0}^{K-1} s(i)$. Therefore, maximizing the utility is equivalent to maximizing the total energy spent over the K slots.

To complete the proof we now show a transformation from an optimal solution $s^*(i)$ to the greedy algorithm's solution $s^g(i)$, which does not decrease the total amount of energy spent over the K slots.

Let i' be the earliest slot for which $s^*(i') \neq s^g(i')$, clearly $s^*(i') < s^g(i')$. Since $s^*(i)$ obtains maximal energy spending, there must be a set S' of slots after slot i' in which the total energy spent is at least $s^g(i') - s^*(i')$. Also note that, due to condition (ii), for some $j > 0$, $s^g(i') - s^*(i') = j \cdot s$. In each of the slots in S' the energy spent is a multiple of s. Therefore, we can reduce the amount of energy spent in S' by $s^g(i') - s^*(i')$ and set $s^*(i') = s^g(i')$. Due to Observation 1 we get a feasible energy spending. Furthermore, at least the $i'+1$ first slots are identical the greedy algorithm's solution. We repeat the process until we obtain the energy spending $s^g(i)$ for $i = 0, \ldots, K-1$. $\square$

Proof of Theorem 4: We set $U(s(i)) = s(i)$, $\eta = 1$, $L(i) = 0$, $C = s_{\min}$ where $s_{\min} = \min\{s \in \mathcal{S}\}$, and $B_0 = B_K = C$. It is sufficient to consider instances in which $e(i) > 0$ only for $i \geq K-2$. Therefore, without loss of generality we assume $K = 2$. Assume that $e(0) = 0$. The online algorithm can: (i) set $s(0) = 0$, or (ii) set $s(0) = s_{\min}$. If the first option is used and $e(1) < s_{\min}$, the solution is infeasible. Thus, to ensure feasibility the online algorithm will set $s(0) = 0$ and similarly $s(1) = 0$, obtaining no utility. Therefore, the performance gap $s_{\min}$ can be arbitrarily large. $\square$

Acknowledgment

References

[1] M. Gorlatova *et al.*, "Movers and shakers: Kinetic energy harvesting for the Internet of things," in *Proc. ACM SIGMETRICS*, Jun. 2014, pp. 407–419.
[2] J. Paradiso and T. Starner, "Energy scavenging for mobile and wireless electronics," *IEEE Pervasive Comput.*, vol. 4, no. 1, pp. 18–27, Jan./Feb. 2005.
[3] M. Gorlatova *et al.*, "Energy-harvesting Active Networked Tags (EnHANTs) for ubiquitous object networking," *IEEE Wireless Commun.*, vol. 17, no. 6, pp. 18–25, Dec. 2010.
[4] A. Kansal, J. Hsu, S. Zahedi, and M. B. Srivastava, "Power management in energy harvesting sensor networks," *ACM Trans. Embedded Comput. Syst.*, vol. 6, no. 4, pp. 32:1–32:38, Sep. 2007.
[5] L. Yerva, B. Campbell, A. Bansal, T. Schmid, and P. Dutta, "Grafting energy-harvesting leaves onto the sensornet tree," in *Proc. IEEE IPSN*, Apr. 2012, pp. 197–207.
[6] J. Gummeson, S. S. Clark, K. Fu, and D. Ganesan, "On the limits of effective micro-energy harvesting on mobile CRFID sensors," in *Proc. ACM MobiSys*, Jun. 2010, pp. 195–208.
[7] R. Vullers, R. van Schaijk, I. Doms, C. Van Hoof, and R. Mertens, "Micropower energy harvesting," *Solid-State Electron.*, vol. 53, no. 7, pp. 684–693, Jul. 2009.
[8] J. Kymissis, C. Kendall, J. Paradiso, and N. Gershenfeld, "Parasitic power harvesting in shoes," in *Proc. IEEE ISWC*, Oct. 1998, pp. 132–139.
[9] G. Lin *et al.*, "Harnessing power through electromagnetic induction utilizing printed coils," U.S. Patent 20 120 235 510, Sep. 2012.
[10] nPower Personal Energy Generator. [Online]. Available: http://www.npowerpeg.com
[11] P. Mitcheson, E. Yeatman, G. Rao, A. Holmes, and T. Green, "Energy harvesting from human and machine motion for wireless electronic devices," *Proc. IEEE*, vol. 96, no. 9, pp. 1457–1486, Sep. 2008.
[12] S. Chen, P. Sinha, N. Shroff, and C. Joo, "A simple asymptotically optimal energy allocation and routing scheme in rechargeable sensor networks," in *Proc. IEEE INFOCOM*, Mar. 2012, pp. 379–387.
[13] M. Gorlatova, A. Wallwater, and G. Zussman, "Networking low-power energy harvesting devices: Measurements and algorithms," *IEEE Trans. Mobile Comput.*, vol. 13, no. 9, pp. 1853–1865, Sep. 2013.
[14] R.-S. Liu, P. Sinha, and C. E. Koksal, "Joint energy management and resource allocation in rechargeable sensor networks," in *Proc. IEEE INFOCOM*, Mar. 2010, pp. 1–9.
[15] Q. Wang and M. Liu, "When simplicity meets optimality: Efficient transmission power control with stochastic energy harvesting," in *Proc. IEEE INFOCOM*, Apr. 2013, pp. 580–584.
[16] J. Yun, S. Patel, M. Reynolds, and G. Abowd, "Design and performance of an optimal inertial power harvester for human-powered devices," *IEEE Trans. Mobile Comput.*, vol. 10, no. 5, pp. 669–683, May 2011.
[17] T. Starner, "Human-powered wearable computing," *IBM Syst. J.*, vol. 35, no. 3/4, pp. 618–629, 1996.
[18] H. Huang, G. Merrett, and N. White, "Human-powered inertial energy harvesters: The effect of orientation, location and activity on obtainable power," in *Proc. Eurosensors*, Sep. 2011, pp. 1–4.
[19] T. Von Buren *et al.*, "Optimization of inertial micropower generators for human walking motion," *IEEE Sensors J.*, vol. 6, no. 1, pp. 28–38, Feb. 2006.
[20] Y. Xue and L. Jin, "A naturalistic 3D acceleration-based activity dataset and benchmark evaluations," in *Proc. IEEE SMC*, Oct. 2010, pp. 4081–4085.
[21] M. Cong *et al.*, CRAWDAD Data set Columbia/Kinetic (v. 2014-05-13), May 2014. [Online]. Available: http://crawdad.cs.dartmouth.edu/columbia/kinetic
[22] T. Buren, P. Lukowicz, and G. Troster, "Kinetic energy powered computing: Experimental feasibility study," in *Proc. IEEE ISWC*, Feb. 2003, pp. 22–24.
[23] EnHANTs Kinetic Energy Measurements, Mar. 2014. [Online]. Available: http://enhants.ee.columbia.edu/kinetic-datasets
[24] *Volture Piezoelectric Energy Harvesters Datasheet*, Mide, Medford, MA, USA, Jan. 23, 2013. [Online]. Available: http://www.mide.com/pdfs/Volture_Datasheet_001.pdf
[25] *Macro Fiber Composite—MFC Datasheet*, Smart Material, Sarasota, FL, USA, 2013. [Online]. Available: http://www.smart-material.com/media/Datasheet/MFC-V2.1-2013-web.pdf
[26] *Piezo Energy Harvester Datasheet*, Piezo Systems, Woburn, MA, USA, 2011. [Online]. Available: http://www.piezo.com/catalog8.pdf
[27] B. Devillers and D. Gunduz, "A general framework for the optimization of energy harvesting communication systems with battery imperfections," *IEEE J. Commun. Netw.*, vol. 14, no. 2, pp. 130–139, Apr. 2012.

[28] D. Noh and T. Abdelzaher, "Efficient flow-control algorithm cooperating with energy allocation scheme for solar-powered WSNs," *Wireless Commun. Mobile Comput.*, vol. 12, no. 5, pp. 379–392, Apr. 2010.

[29] T. Zhu, Z. Zhong, Y. Gu, T. He, and Z.-L. Zhang, "Leakage-aware energy synchronization for wireless sensor networks," in *Proc. ACM MobiSys*, Jun. 2009, pp. 319–332.

[30] M. Orendurff, J. Schoen, G. Bernatz, A. Segal, and G. Klute, "How humans walk: Bout duration, steps per bout, rest duration," *J. Rehab. Res. Dev.*, vol. 45, no. 7, pp. 1077–1089, 2008.

[31] J. Yang and S. Ulukus, "Optimal packet scheduling in an energy harvesting communication system," *IEEE Trans. Commun.*, vol. 60, no. 1, pp. 220–230, Jan. 2012.

[32] O. Ozel, K. Tutuncuoglu, J. Yang, S. Ulukus, and A. Yener, "Transmission with energy harvesting nodes in fading wireless channels: Optimal policies," *IEEE J. Sel. Areas Commun.*, vol. 29, no. 8, pp. 1732–1743, Sep. 2011.

[33] N. Michelusi, K. Stamatiou, and M. Zorzi, "Transmission policies for energy harvesting sensors with time-correlated energy supply," *IEEE Trans. Commun.*, vol. 61, no. 7, pp. 2988–3001, Jul. 2013.

[34] O. Orhan, D. Gunduz, and E. Erkip, "Optimal packet scheduling for an energy harvesting transmitter with processing cost," in *Proc. IEEE ICC*, Jun. 2013, pp. 3110–3114.

[35] S. Beeby, M. Tudor, and N. White, "Energy harvesting vibration sources for microsystems applications," *Meas. Sci. Technol.*, vol. 17, no. 12, p. R175, Dec. 2006.

[36] *LTC3588 Piezoelectric Energy Harvesting Power Supply Datasheet*, Linear Technology, Milpitas, CA, USA, 2010. [Online]. Available: http://cds.linear.com/docs/en/datasheet/35881fb.pdf

[37] M. Zafer and E. Modiano, "A calculus approach to energy-efficient data transmission with quality-of-service constraints," *IEEE/ACM Trans. Netw.*, vol. 17, no. 3, pp. 898–911, Jun. 2009.

[38] M. Gorlatova *et al.*, "Prototyping Energy Harvesting Active Networked Tags (EnHANTs)," in *Proc. IEEE INFOCOM, Mini-Conf.*, Apr. 2013, pp. 585–589.

[39] M. C. Domingo, "Packet size optimization for improving the energy efficiency in body sensor networks," *ETRI J.*, vol. 33, no. 3, pp. 299–309, Jun. 2011.

[40] G. V. Merrett *et al.*, "An empirical energy model for supercapacitor powered wireless sensor nodes," in *Proc. IEEE ICCCN*, Aug. 2008, pp. 1–6.

[41] J. Galloway, *Pick up the Beat*. Emmaus, PA, USA: Runners World, Jul. 2007. [Online]. Available: http://www.runnersworld.com/running-tips/pick-beat

[42] L. Huang and M. Neely, "Utility optimal scheduling in energy harvesting networks," *IEEE/ACM Trans. Netw.*, vol. 21, no. 4, pp. 1117–1130, Aug. 2013.

[43] *CC2420 2.4gGHz IEEE802.15.4/ZigBee-ready RF Transceiver Datasheet*, Chipcon, Dallas, TX, USA, Nov. 2013. [Online]. Available: http://www.ti.com/lit/ds/symlink/cc2420.pdf

[44] *LTM4607 36 V_IN, 24 V_OUT High Efficiency Buck-Boost DC/DC μModule Regulator*, Linear Technology, Milpitas, CA, USA, 2008. [Online]. Available: {http://cds.linear.com/docs/en/datasheet/4607fc.pdf

[45] *Si7013-A10 I2C Humidity and Two-Zone Temperature Sensor*, Silicon Labs., Austin, TX, USA, 2014. [Online]. Available: http://www.silabs.com/Support%20Documents/TechnicalDocs/Si7013.pdf

[46] O. Ozel and S. Ulukus, "Achieving awgn capacity under stochastic energy harvesting," *IEEE Trans. Inf. Theory*, vol. 58, no. 10, pp. 6471–6483, Oct. 2012.

[47] H. Kellerer, U. Pferschy, and D. Pisinger, *Knapsack Problems*. Berlin, Germany: Springer-Verlag, 2004.

John Sarik received the B.S. degree from The University of Texas, Austin, TX, USA, and the M.S. and Ph.D. degrees from Columbia University, New York, NY, USA, all in electrical engineering. He has cofounded several start-up companies, including Radiator Labs and Lumiode. He is currently with Xenex Disinfection Services, San Antonio, TX.

Guy Grebla received the B.A. and M.A. degrees and the Ph.D. degree in 2013 from Technion—Israel Institute of Technology, Haifa, Israel, all in computer science. He is currently a Postdoctoral Research Scientist with the Department of Electrical Engineering, Columbia University, New York, NY, USA.

Mina Cong received the B.Sc. degree in electrical engineering from Columbia University, New York, NY, USA, in December 2014. She is currently an Applications Developer at AT&T, Bothell, WA, USA.

Ioannis Kymissis (SM'10) received the S.B., M.Eng., and Ph.D. degrees from Massachusetts Institute of Technology, Cambridge, MA, USA. In 2006, he joined the faculty of the Department of Electrical Engineering, Columbia University, New York, NY, USA, where he currently heads the Columbia Laboratory for Unconventional Electronics, which is developing a variety of thin-film sensing, display, and actuation systems.

Maria Gorlatova received the B.Sc. and M.Sc. degrees from the University of Ottawa, Ottawa, ON, Canada, and the Ph.D. degree from Columbia University, New York, NY, USA, all in electrical engineering. She is currently a Program Manager at D. E. Shaw Research, New York. Dr. Gorlatova has been a recipient of Canadian Graduate Scholar CGS NSERC Fellowships, The Google Anita Borg USA Fellowship, and the IEEE Communications Society Award for Advances in Communications.

Gil Zussman (S'02–M'05–SM'07) received the Ph.D. degree in electrical engineering from Technion - Israel Institute of Technology, Haifa, Israel, in 2004. He was a Postdoctoral Associate with Massachusetts Institute of Technology in 2004–2007. He is currently an Associate Professor of electrical engineering with Columbia University, New York, NY, USA. He is a corecipient of five paper awards, including the ACM SIGMETRICS'06 Best Paper Award and the 2011 IEEE Communications Society Award for Outstanding Paper on New Communication Topics. He received the Fulbright Fellowship, the DTRA Young Investigator Award, and the NSF CAREER Award, and he was a member of a team that won first place in the 2009 Vodafone Foundation Wireless Innovation Project Competition.